

Supporting Information

Synthesis of β -(Hetero)aryl Ketones *via* Ligand-Enabled Nondirected C–H Alkylation

Yogesh Bairagi,^{1‡} Sandip Porey,^{1‡} Sai V. C. Vummaleti,² Xinglong Zhang,^{2,3*} Goutam Kumar Lahiri^{1*} & Debabrata Maiti^{1*}

¹Department of Chemistry, Indian Institute of Technology Bombay, Powai, Mumbai 400076, India

²Institute of High Performance Computing (IHPC), Agency for Science, Technology and Research (A*STAR), 1 Fusionopolis Way, #16-16 Connexis, Singapore 138632, Republic of Singapore

³Department of Chemistry, The Chinese University of Hong Kong, Shatin, New Territories, Hong Kong, China

E-mail: dmaiti@chem.iitb.ac.in

E-mail: lahiri@chem.iitb.ac.in

E-mail: zhang_xinglong@ihpc.a-star.edu.sg

Table of Contents

Experimental section part-I

1. General consideration	S4
1.1 Reagent Information	S4
1.2 Analytical Information	S4
1.3 Description of reaction tube	S4
2. Experimental Section	S5
2.1 General procedure for synthesis of carbonyl ester	S5
2.2 General procedure for synthesis of aliphatic long chain allyl alcohol	S5
2.3 Optimization details	S6
2.4 General procedure: Synthesis of β -(Hetero)aryl Ketones Ligand-Enabled Nondirected C–H Alkylation	S14
2.5 Application: the further transformation of the protocol	S16
2.6 Determination of yield and selectivity	S17
2.7 Gram scale synthesis of 1-(naphthalen-2-yl)pentan-3-one	S18
2.8 Unsuccessful substrate and allyl alcohol	S19
3. Mechanistic investigations	S20
3.1 Synthesis and Characterization of d2-benzothiophene	S20
3.2 Mechanistic Investigations	S20-S28
4. Mass analysis for C–H activated intermediate	S28-S29
4.1 Proposed mechanistic cycle for Synthesis of β -(Hetero)aryl Ketones via Ligand-Enabled Nondirected C-H Alkylation.	S30
5. Characterization data	S31-S62
6. NMR spectra	S63-S131
6.1 ^1H -NMR data of crude reaction mixture	S132-S134
7. Crystal data	S135-S137
7.1. References	S138

Computational section: part II

8. Computational methods	S140
9. Model Reaction	S141
10. Possible conformers of C–H activation transition states (TSs) via concerted metalation deprotonation (CMD)	S141
11. C–H activation with different ligand binding mode	S143
12. Role of Ag_2CO_3 in the 1,2-migratory insertion step	S144
13. β -H and β' -H transfer TS structures: <i>cis</i> vs. <i>trans</i> conformers	S145
14. Product release from intermediate a-INT5	S147
15. Formation of Pd(0) species: $\text{CuF}_2 \cdot 2\text{H}_2\text{O}$ vs Ag_2CO_3	S148
16. Pathway for the formation of minor olefin product)	S150

17. DFT optimized crucial transition state structures (TSs)	S152
18. Optimized structures and absolute energies	S153
19. References for computational section	S155

Experimental Section- Part I

Computational section: part II

8. Computational Methods:

Density functional theory (DFT) calculations were performed with *Gaussian 16* rev. B.01.¹ Geometry optimizations were initially performed using the global-hybrid meta-NGA (nonseparable gradient approximation) MN15 functional² with the def2-SVP^{3,4} Karlsruhe-family basis set and the optimized structures further refined with a mix of larger basis set consisting of triple- ζ valence def2-TZVPPD (where ‘D’ indicates diffuse basis functions) for Pd^{5,6} and Ag^{5,6} atom and def2-SVP^{3,4} for all other atoms (BS1). Minima and transition structures on the potential energy surface (PES) were confirmed using harmonic frequency analysis at the same level of theory, showing respectively zero and one imaginary frequency.

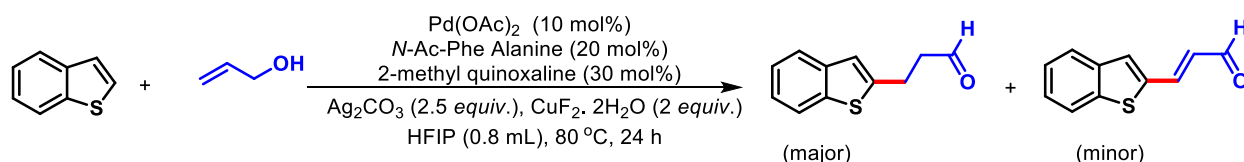
Single point (SP) corrections were performed using MN15 functional and def2-QZVP³ basis set for all atoms. The SMD implicit continuum solvation model⁷ was used to account for the effect of hexafluoroisopropanol (HFIP) solvent on the computed Gibbs energy profile. Since HFIP solvent is not available in the list of default/pre-defined solvents in the *Gaussian 16* software, it is herein parametrised using a set of *seven* parameters.⁷ These include 1) the static dielectric constant of the solvent at 25°C ($Eps = 16.7$);⁸⁻¹⁰ 2) dynamic (optical) dielectric constant – the square of the refractive index value of 1.275 at 20°C was used¹¹ ($EpsInf = 1.625625$); 3) hydrogen bond acidity ($HBondAcidity = 0.77$)¹² and 4) hydrogen bond basicity ($HBondBasicity = 0.10$)¹², which are Abraham’s *A* and *B* values respectively; 5) the surface tension of the solvent at interface ($SurfaceTensionAtInterface = 23.23$)¹³ – this value is obtained from the conversion of the surface tension of HFIP at 16.14 mN/m at 25°C¹⁴ to $\text{cal mol}^{-1} \text{ \AA}^{-2}$ used in the SMD model by the conversion factor of $1 \text{ dyne/cm} = 1 \text{ mN/m} = 1.43932 \text{ cal mol}^{-1} \text{ \AA}^{-2}$ as outlined in the Truhlar’s Minnesota Solvent Descriptor Database¹⁵; 6) carbon aromaticity – the fraction of aromatic carbons ($CarbonAromaticity = 0.00$) and 7) electronegative halogenicity – the fraction of halogens ($Electronegative Halogenicity = 0.60$). These parameters were specified using the keyword “SCRF = (SMD, Solvent= Generic, Read)” in *Gaussian 16*.

Gibbs energies were evaluated at the reaction temperature of 353.15 K (80°C), using a quasi-RRHO treatment of vibrational entropies.^{16,17} Vibrational entropies of frequencies below 100 cm^{-1} were obtained according to a free rotor description, using a smooth damping function to interpolate between the two limiting descriptions. The free energies were further corrected

using standard concentration of 1 mol/L, which were used in solvation calculations. Unless otherwise stated, the final SMD (HFIP)-MN15/def2-QZVP//MN15/BS1 Gibbs energies are used for discussion throughout. *All Gibbs energy values in the text and figures are quoted in kcal mol⁻¹.* All molecular structures and molecular orbitals were visualized using *PyMOL* software.¹⁸

9. Model reaction:

In this study, we select the model reaction depicted in Scheme S1 for in-depth mechanistic investigations using DFT modeling.



Scheme S1. Model reaction used for DFT based mechanistic studies.

10. Possible conformers of C–H activation transition states (TSs) via concerted metalation deprotonation (CMD)

We have explored various possible conformations for the crucial C–H activation step transition state **TS1**, with **a-TS1** corresponding to C₂–H activation and **b-TS1** representing the C₃–H activation, Figures S2 and S3, respectively. Our computational results show that **a-TS1** is the most stable conformer, with a stability difference of 0.8–1.9 kcal mol⁻¹ compared to its other conformers (**a-TS1'**, **a-TS1''**, and **a-TS1'''**) (Figure S2), and it exhibits higher stability by 0.9–2.1 kcal mol⁻¹ than the competing transition state **b-TS1** and its conformers (**b-TS1'**, **b-TS1''**, and **b-TS1'''**) (Figure S3).

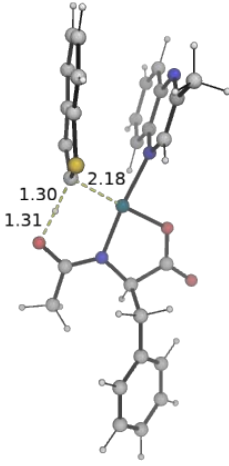
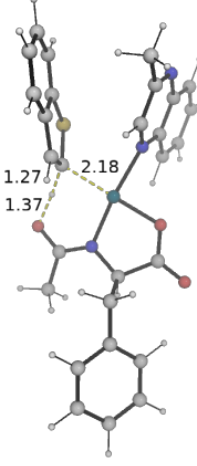
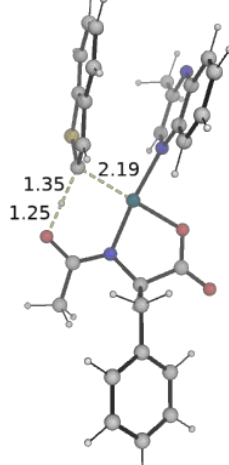
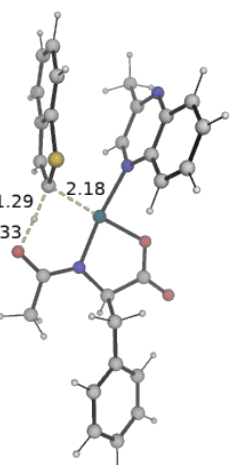
a-TS1	a-TS1'
$\Delta G^\ddagger = 0.0 \text{ kcal mol}^{-1}$	$\Delta G^\ddagger = 0.8 \text{ kcal mol}^{-1}$
	
a-TS1''	a-TS1'''
$\Delta G^\ddagger = 1.2 \text{ kcal mol}^{-1}$	$\Delta G^\ddagger = 1.9 \text{ kcal mol}^{-1}$
	

Figure S2. DFT optimized possible conformers of C₂-H activation transition states. The Gibbs activation free energy values (in kcal mol⁻¹) are given relative to the most stable TS, **a-TS1**.

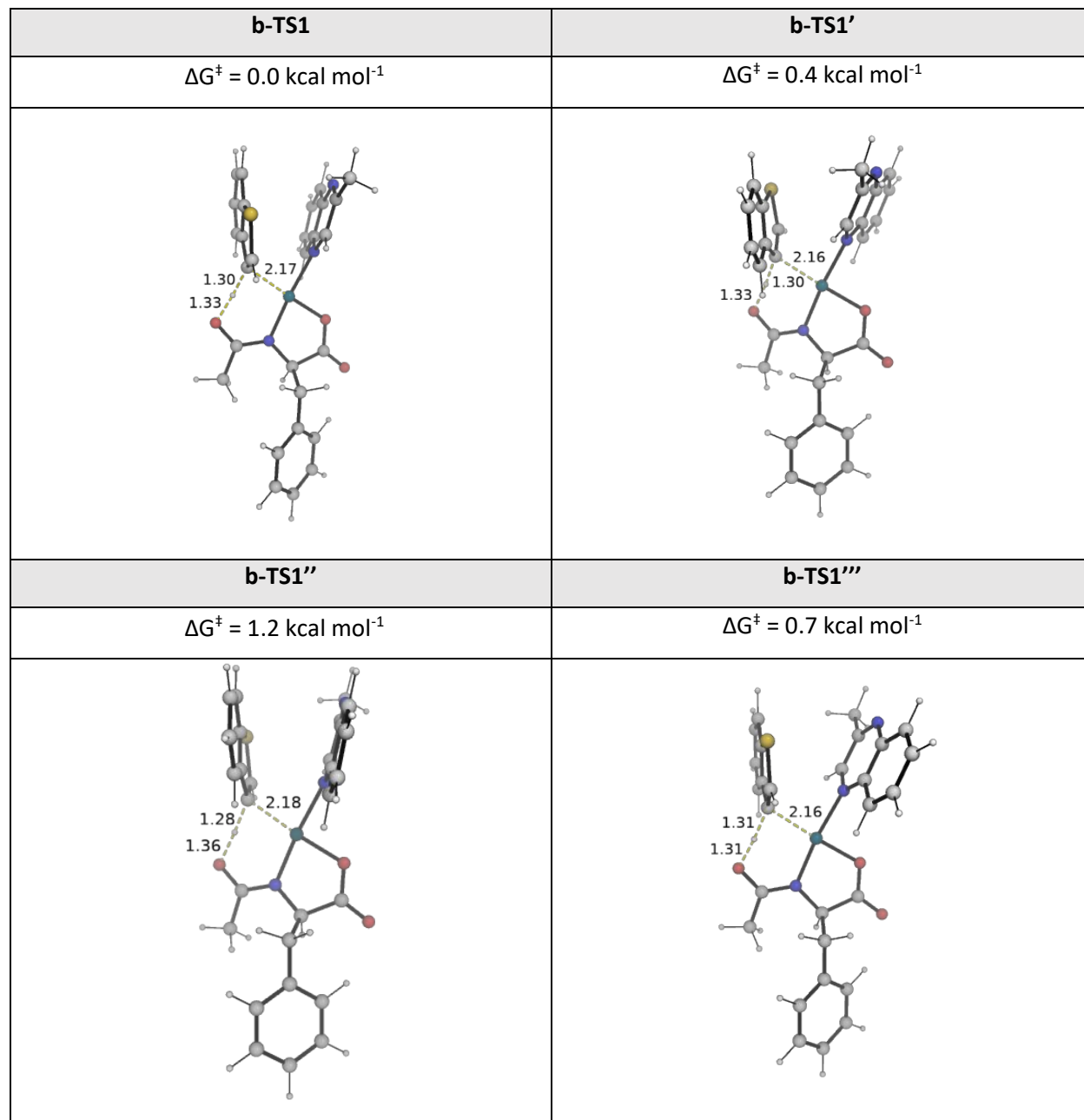


Figure S3. DFT optimized possible conformers of C₃-H activation transition states. The Gibbs activation free energy values (in kcal mol⁻¹) are given relative to the most stable TS, **b-TS1**.

11.C-H activation with different ligand binding mode

We explored an alternative configuration of the C-H activation step where the ligand binds via the other N atom, different from that in **a-TS1**. In this configuration, referred to as **a-TS1a**, 2-methoxy quinoxaline ligand coordinates to the Pd center via the nitrogen atom at the α -position to the methyl substituent, Figure S4. Our DFT calculations suggest that the C₂-H activation via

a-TS1a is less favorable than **a-TS1** by 1.5 kcal mol⁻¹, indicating that this alternative pathway is less kinetically preferred.

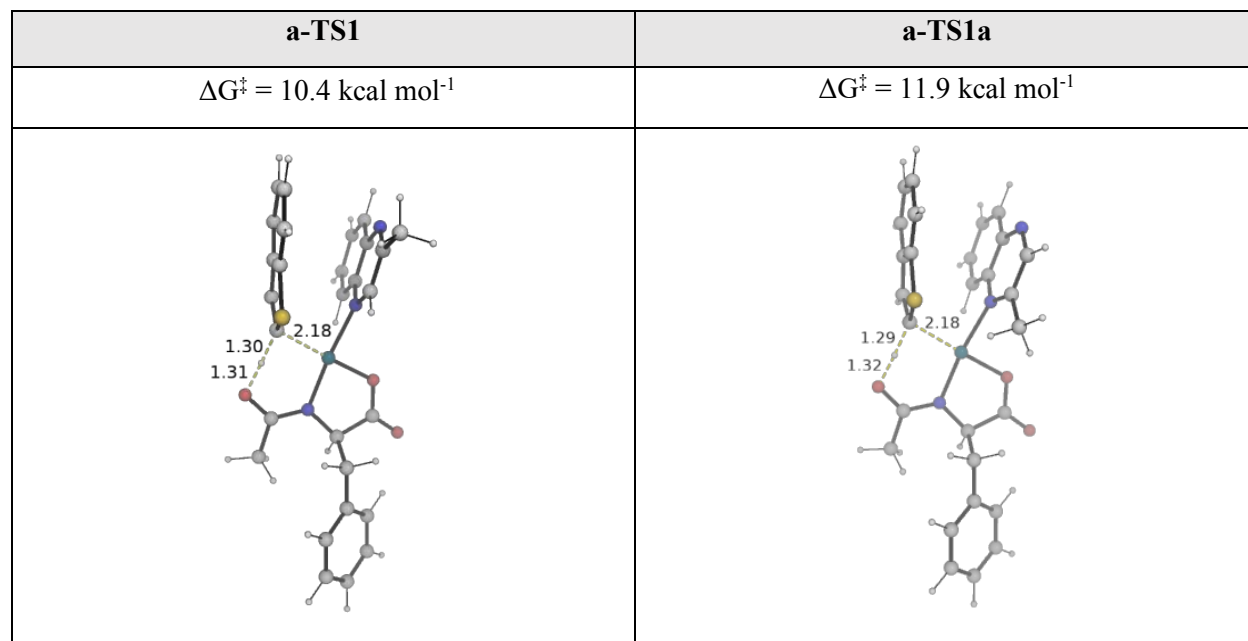


Figure S4. DFT optimized geometries of the C₂-H activation transition states with different ligand binding modes. The Gibbs reaction and activation free energies are (given in kcal mol⁻¹) relative to the starting catalyst catalyst Pd(OAc)₂.

12. Role of Ag₂CO₃ in the 1,2-migratory insertion step

Alternatively, from **a-INT3**, we have explored 1,2-migratory insertion assisted by silver carbonate (Ag₂CO₃), Figure S5. In the presence of Ag₂CO₃, our results suggest that the overall estimated barrier, **a-TS2_Ag** (13.5 kcal mol⁻¹ above **INT1**), is lower by only 0.5 kcal mol⁻¹ to that of **a-TS2**, (14.0 kcal mol⁻¹ above **INT1**), where Ag₂CO₃ is absent, Figure 1 of the main text and Figure S5. These findings are supported by the minor changes (< 5 pm) observed in the calculated crucial distances of Pd-C and C-C bond distances, implying that Ag₂CO₃ may not have significant role in influencing the studied 1,2-migratory insertion step.

a-TS2	a-TS2_Ag
$\Delta G^\ddagger = 14.0 \text{ kcal mol}^{-1}$	$\Delta G^\ddagger = 13.5 \text{ kcal mol}^{-1}$

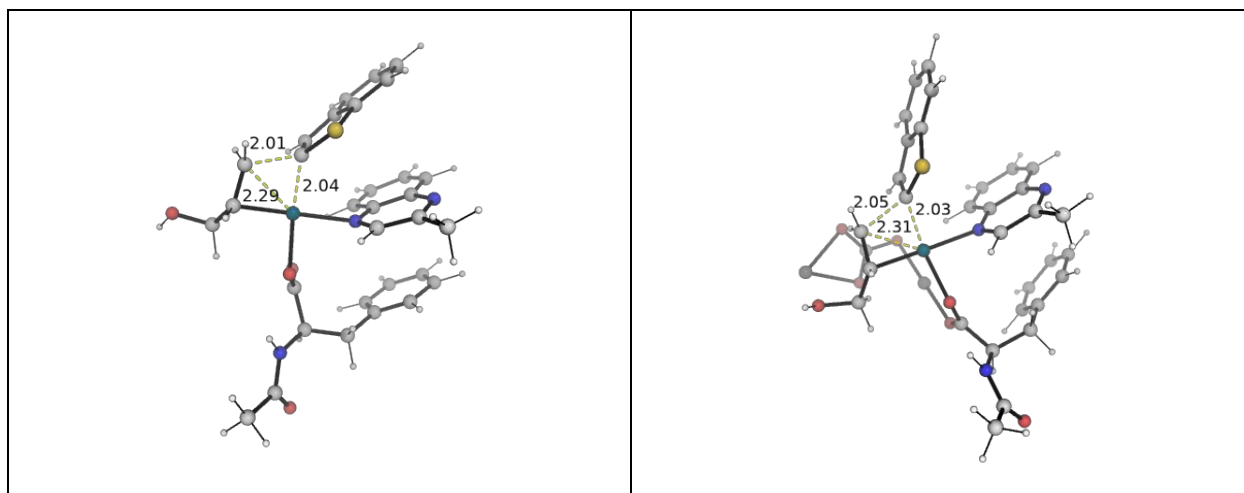
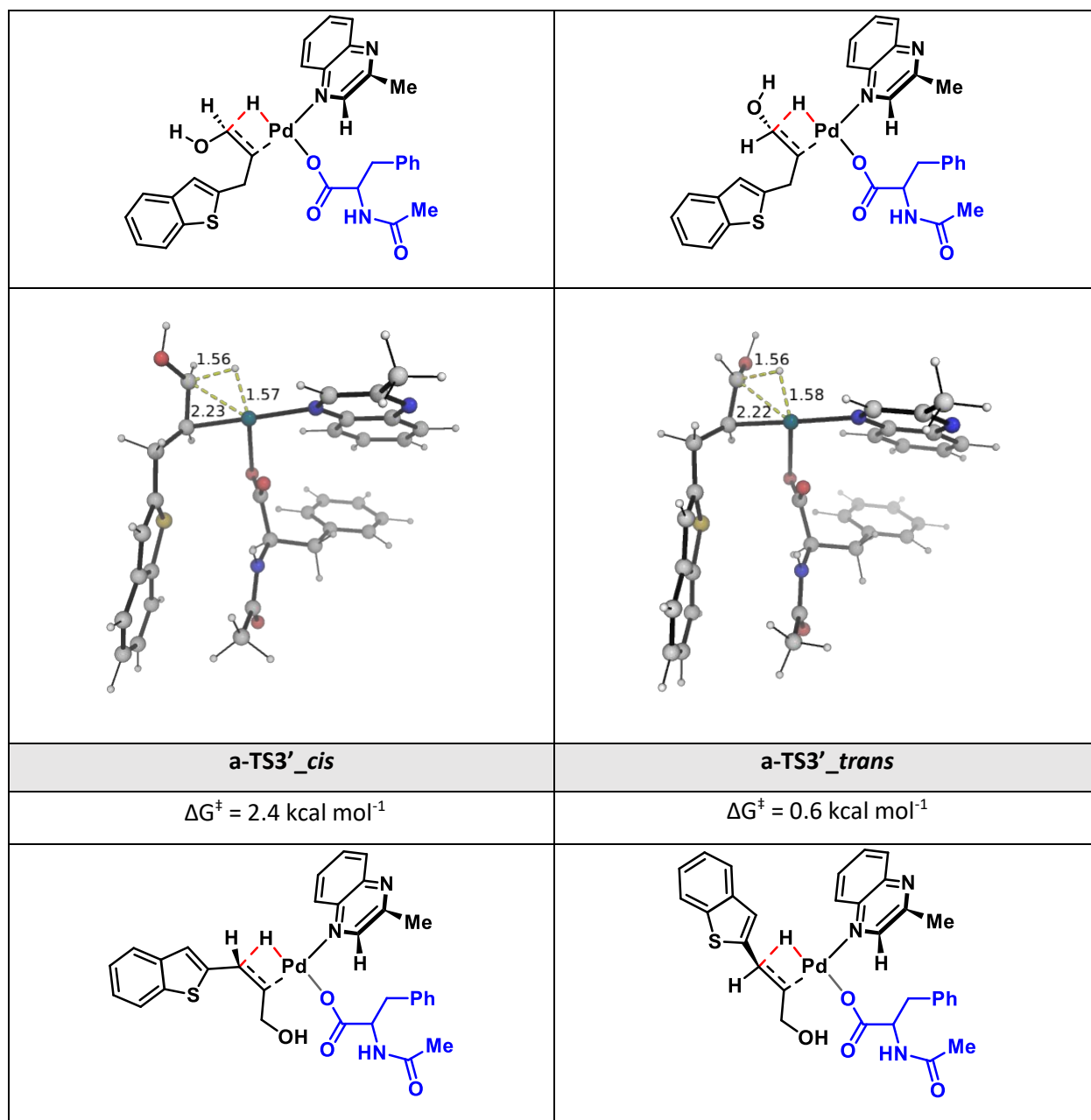


Figure S5. DFT optimized transition state structures for the 1,2-migratory insertion step, without Ag_2CO_3 , **a-TS2**, and in the presence of Ag_2CO_3 , **a-TS2_Ag**. The Gibbs free energy barrier values (in kcal mol^{-1}) are given relative to the stable intermediate **INT1**.

13. β -H and β' -H transfer TS structures: *cis* vs. *trans* conformers

From **a-INT4**, we have explored the transfer of both H atoms from β and β' positions to the metal Pd center, resulting in *cis* and *trans* conformations for the corresponding TS structures, **a-TS3** and **a-TS3'**, Figures S6. From **a-INT4**, the calculated TS barriers for β -H transfer reaction reveal that the *cis* conformer, **a-TS3_cis**, is more favorable by $1.2 \text{ kcal mol}^{-1}$ compared to the *trans* conformer, **a-TS3_trans**, Figure S6. On the other hand, for β' -H transfer reaction, the computed TS barrier for the *trans* conformer, **a-TS3'_trans**, is lower in energy by $1.8 \text{ kcal mol}^{-1}$ compared to *cis* conformer, **a-TS3'_cis**. Overall, the calculated TS barriers suggest that β -H transfer via **a-TS3_cis** has the lowest activation barrier, which is lower in energy by $0.6 \text{ kcal mol}^{-1}$ compared to β' -H transfer via **a-TS3'_trans**, and is therefore predicted to be kinetically most favorable.

a-TS3_cis	a-TS3_trans
$\Delta G^\ddagger = 0.0 \text{ kcal mol}^{-1}$	$\Delta G^\ddagger = 1.2 \text{ kcal mol}^{-1}$



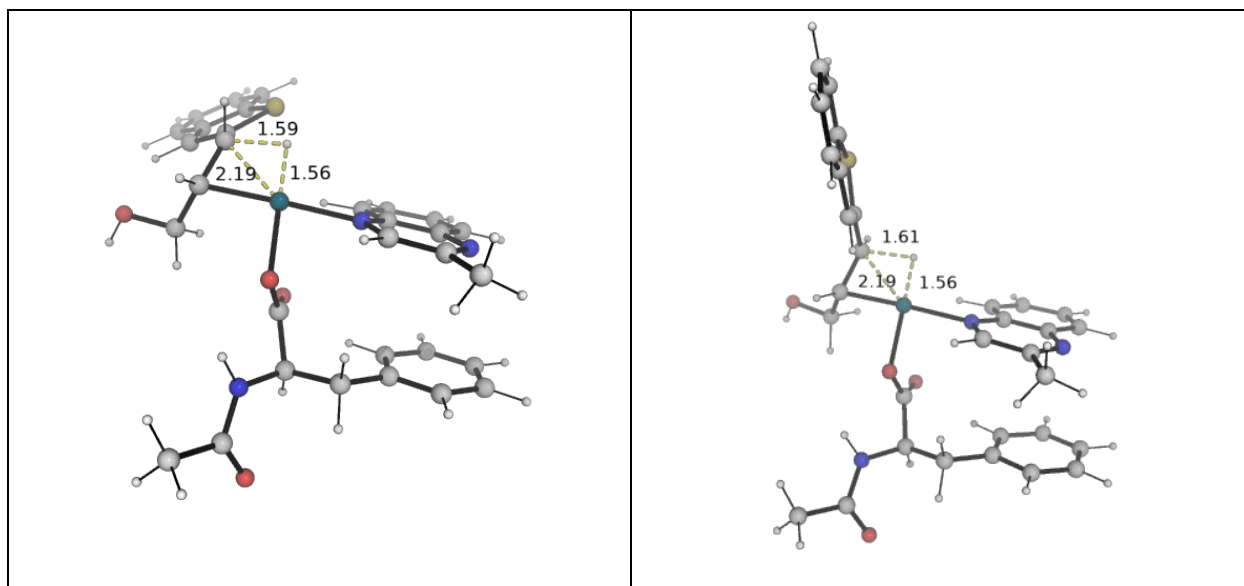
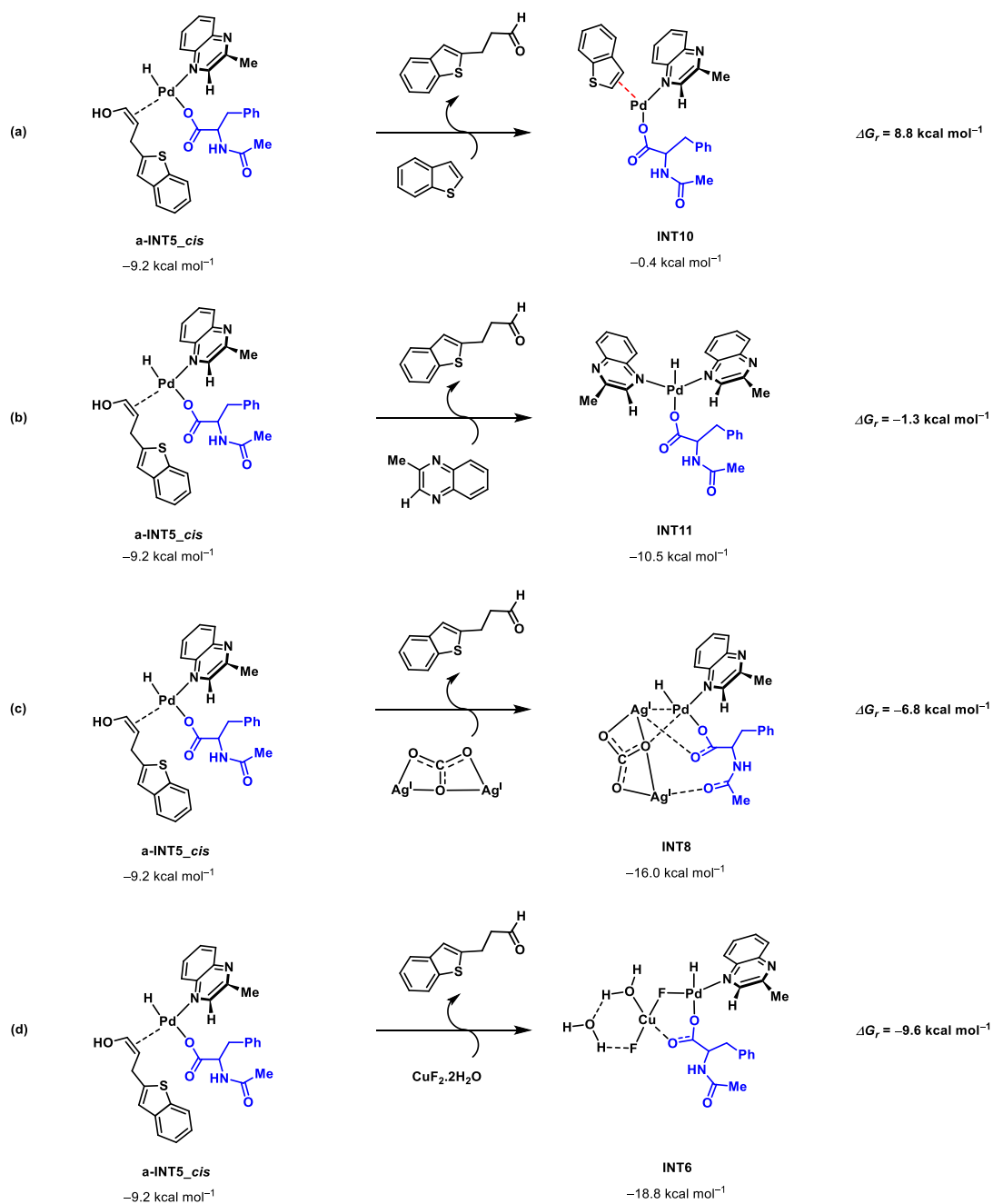


Figure S6. DFT optimized *cis* and *trans* conformers of the transition state structures for the β -H (**a-TS3**) and β' -H (**a-TS3'**) transfer step. The Gibbs activation free energy values (in kcal mol⁻¹) are given relative to the most stable TS, **a-TS3_cis** for the β -H transfer step.

14. Product release from intermediate **a-INT5_cis**

In this section, we explore various possibilities for releasing the alkylated product from intermediate **a-INT5_cis**, Scheme S2.

Firstly, the release of the alkyl product from **a-INT5_cis** with the substitution of one molecule of benzothiophene (Scheme S2a) leads to **INT10**, which is uphill by 8.8 kcal mol⁻¹, rendering it an unfavorable process. Alternatively, using a 2-methyl quinoxaline ligand to displace the product from **a-INT5_cis** (Scheme S2b) results in the formation of **INT11**, which is slightly downhill by -1.3 kcal mol⁻¹. Furthermore, using Ag₂CO₃ salt to displace the product (Scheme S2c), leads to the formation of a more thermodynamically stable Pd-Ag species **INT8**, which is downhill by 6.8 kcal mol⁻¹. Finally, when CuF₂·2H₂O is used to displace the product (Scheme S2d), it forms the most thermodynamically stable Pd-F-Cu species **INT6**, which is downhill by 9.6 kcal mol⁻¹, making it the most favorable process.

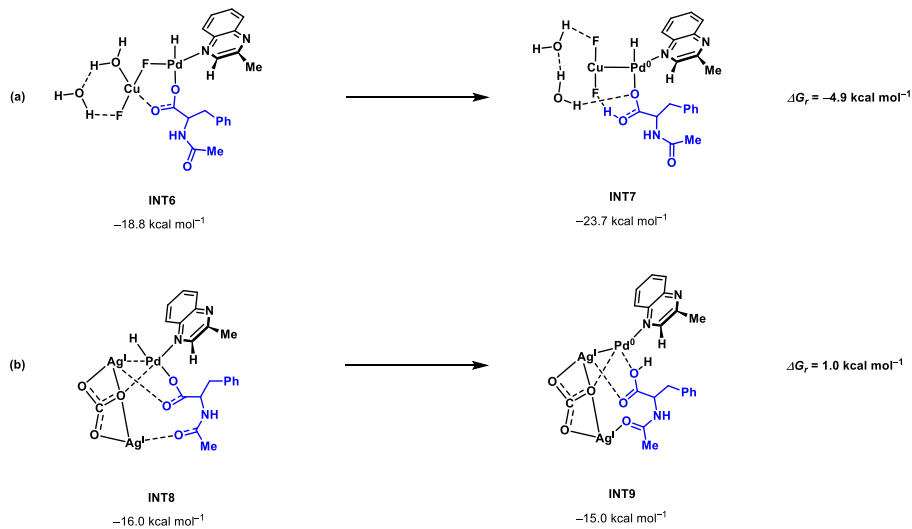


Scheme S2. Thermodynamics for the release of alkyl product from **a-INT5_cis**. Note that the free energy of the Ag_2CO_3 monomer is considered as half of its dimer's computed free energy.

15. Formation of Pd(0) species: $\text{CuF}_2 \cdot 2\text{H}_2\text{O}$ vs Ag_2CO_3

When using $\text{CuF}_2 \cdot 2\text{H}_2\text{O}$, the formation of Pd(0) species **INT7** from **INT6** via a reductive elimination step is exergonic, lying $4.9 \text{ kcal mol}^{-1}$ below **INT6**, Scheme S3. In contrast, with

Ag_2CO_3 , the formation of Pd(0) species **INT9** is endergonic, lying $1.0 \text{ kcal mol}^{-1}$ above **INT8**, suggesting that $\text{CuF}_2 \cdot 2\text{H}_2\text{O}$ forms a more stable Pd(0) species compared to Ag_2CO_3 .



Scheme S3. Formation of Pd(0) species assisted by a) $\text{CuF}_2 \cdot 2\text{H}_2\text{O}$, and b) Ag_2CO_3 . Note that the free energy of the Ag_2CO_3 monomer is considered as half of its dimer's computed free energy.

16. Pathway for the formation of minor olefin product

In this section, we explore an alternative pathway from **a-INT5_{cis}**, leading to the formation of a minor olefin product, Scheme S1 and Figure S7. In detail, from **a-INT5_{cis}**, the transfer β -H to the Pd center leads to intermediate **a-INT6**, proceeding through **a-TS4** with an activation free energy barrier of 26.7 kcal mol⁻¹ (or a significant overall energy barrier of 39.4 kcal mol⁻¹ above **a-INT4**), Figure S7. This reaction is endergonic with **a-INT6** lying at 13.5 kcal mol⁻¹ above **a-INT5_{cis}**, Figure S7. Subsequently, the removal of H₂ molecule from **a-INT6** is exergonic by 15.9 kcal mol⁻¹, leading to the formation of Pd-allyl intermediate **a-INT7**, Figure S7. Next, the transfer of a hydride from the OH group in **a-INT7** to the Pd metal center results in the formation of intermediate **a-INT8**, where the olefin product is coordinated to the Pd metal center, Figure S7. This step proceeds through transition state **a-TS5** and requires overcoming a significant free energy barrier of 40.1 kcal mol⁻¹ above the stable intermediate **a-INT4**. Finally, removal of the product from **a-INT8**, assisted by CuF₂·2H₂O, forms **INT6'**, and the subsequent reductive elimination leading to **INT7'**, followed by a redox reaction regenerates the starting Pd(II) catalyst.

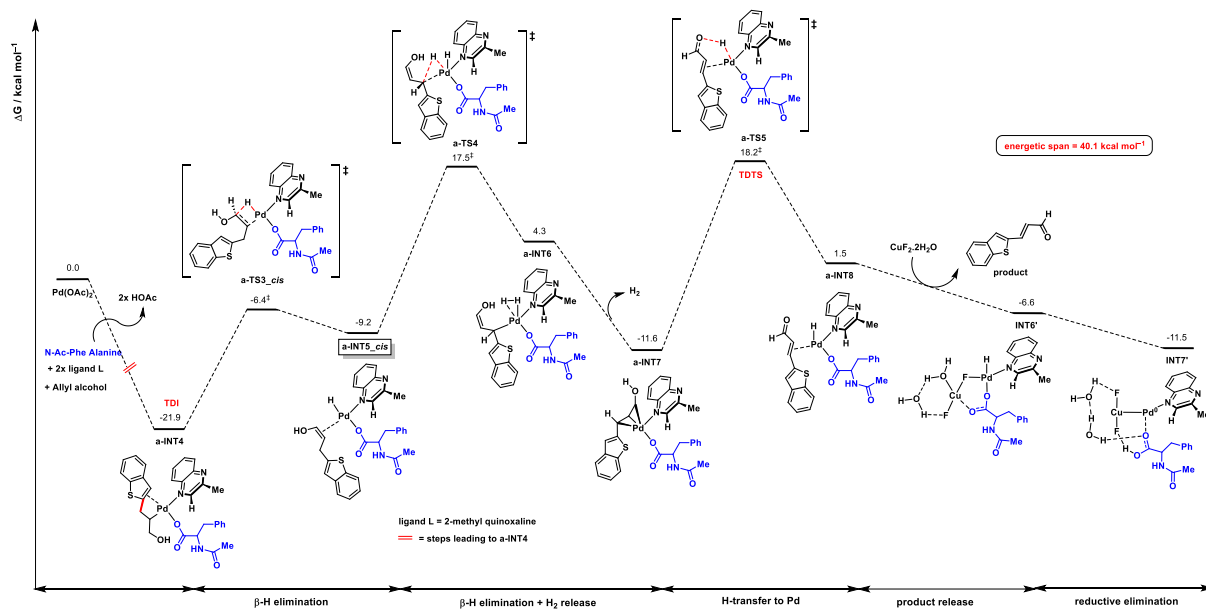
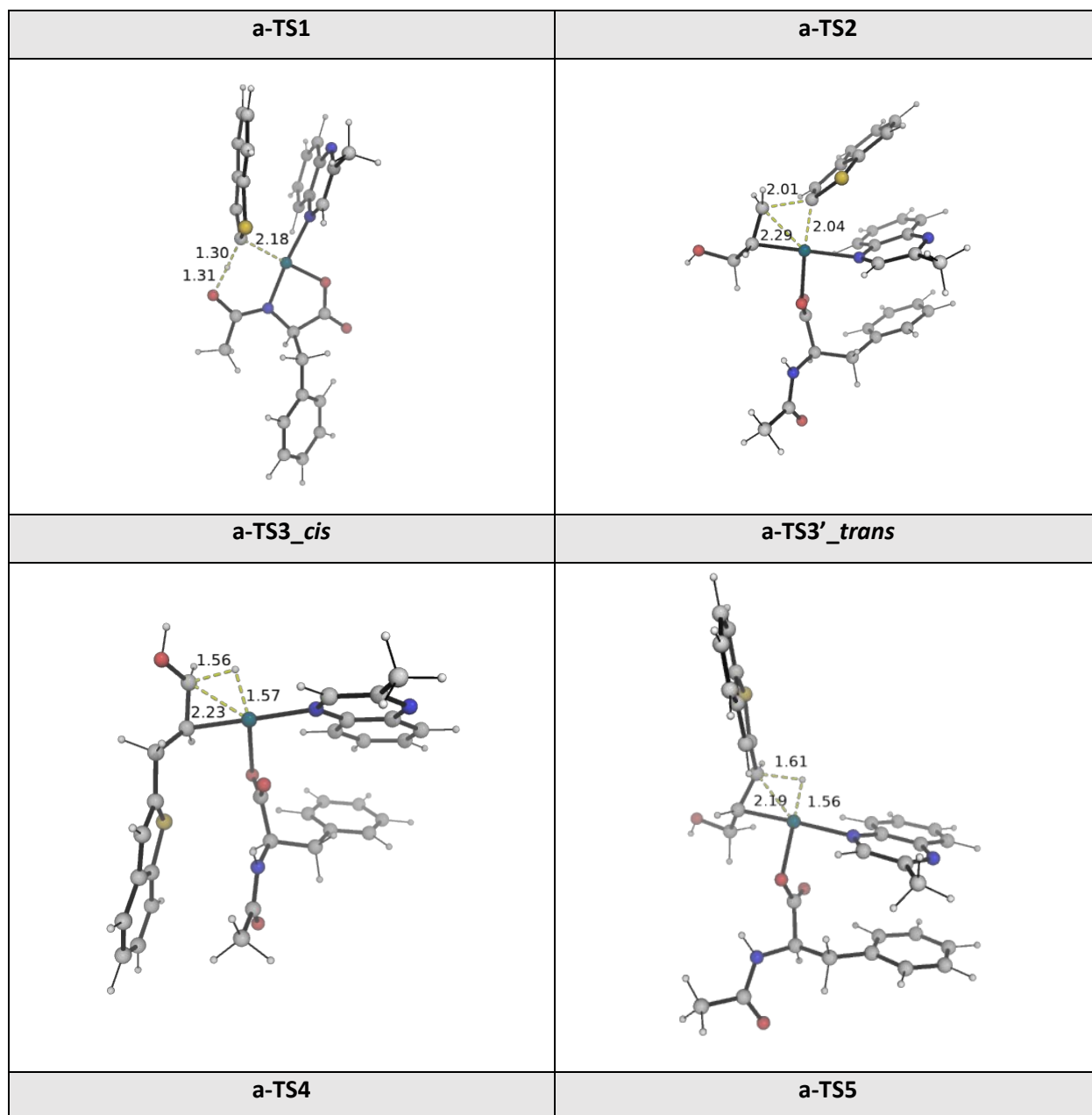


Figure S7. Gibbs free energy profile for the pathway leading to minor olefin product starting from most stable intermediate **a-INT5_{cis}**. The free energies computed at SMD(HFIP)-MN15/def2-QZVP//MN15/(def2-TZVPPD for Pd, Ag + def2-SVP for all other atoms). All values are given in kcal mol⁻¹ with respect to starting catalyst Pd(OAc)₂, and all other substrates. TDI = Turnover-frequency Determining Intermediate, TDTS = Turnover-frequency Determining Transition State.

From Figure S7, it is evident that **a-TS5** exhibits the highest barrier among all the steps in the catalytic cycle, making it the TDTS, while **a-INT4** represents the TDI, being the most stable intermediate in the studied catalytic cycle. The catalytic cycle exhibits an overall energetic span (δE) of 40.1 kcal mol⁻¹, which is significantly higher than the calculated δE of 23.6 kcal mol⁻¹ for the alkylated product cycle, thus providing a possible explanation for the observed olefin product as a minor product, Figure 1 of the main text and Figure S7.

17. DFT optimized crucial transition state structures (TSs)



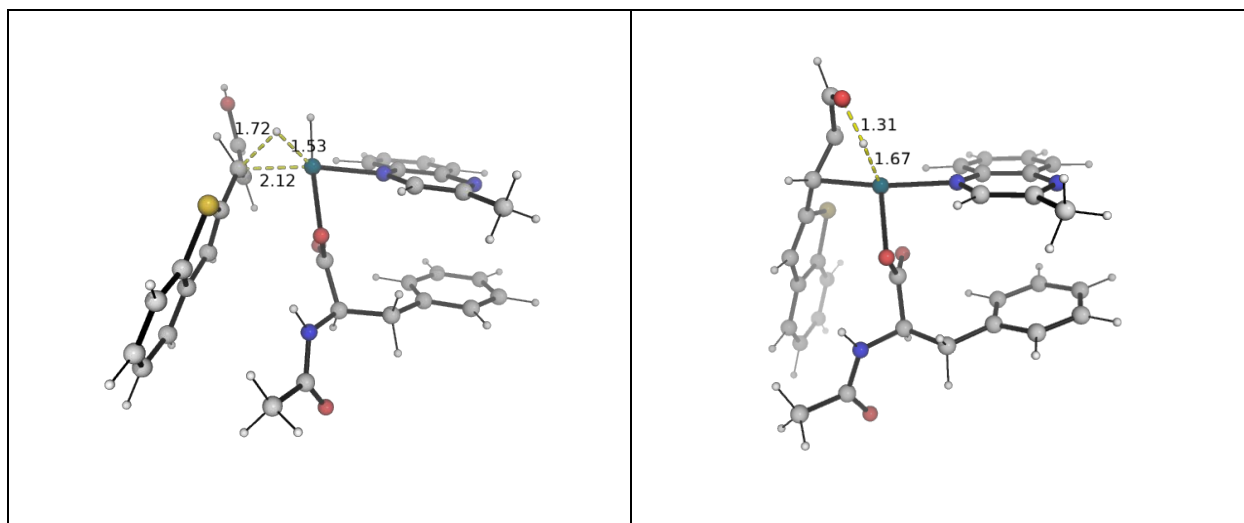


Figure S8. DFT optimized crucial transition state structures for the studied steric-controlled alkylation mechanism catalyzed by Pd(OAc)₂, using benzothiophene as a substrate.

18. Optimized structures and absolute energies,

Geometries of all optimized structures (in .xyz format with their associated energy in Hartrees) are included in a separate folder named *DFT_optimized_structures*. All these data have been deposited and uploaded to zenodo.org under <https://zenodo.org/records/13736351> (DOI: 10.5281/zenodo.13736351).

Absolute values (in Hartrees) for SCF energy, zero-point vibrational energy (ZPE), enthalpy and quasi-harmonic Gibbs free energy (at 80°C/353.15 K) for optimized structures are given below. Single point corrections in SMD hexafluoroisopropanol (HFIP) using MN15/def2-QZVP level of theory are also included.

Structure	E/au	ZPE/au	H/au	T.S/au	qh-G/au	SP MN15/def2-QZVP
2-metquinoxaline	-456.336192	0.152089	-456.171442	0.050729	-456.221535	-457.17118
H₂	-1.161085	0.010237	-1.146933	0.01445	-1.161384	-1.170285
HOAc	-228.644533	0.062197	-228.575319	0.036448	-228.611431	-229.064576
N-Ac-Phenyl alanine	-706.046474	0.228529	-705.797308	0.07206	-705.864968	-707.3377621
Pd(OAc)₂	-583.809931	0.104327	-583.69077	0.058986	-583.746967	-584.634037
allylalcohol	-192.715366	0.085284	-192.62243	0.037183	-192.659594	-193.083054

CuF₂·2H₂O	-1992.780618	0.054891	-1992.71412	0.049566	-1992.76284	-1993.539747
Ag₂CO₃_dimer	-1113.572915	0.036678	-1113.51634	0.077449	-1113.58873	-1114.551126
Ag₂CO₃	-556.7864575	0.018339	-556.75817	0.0387245	-556.794365	-557.275563
Ag_allylcohol	-749.507602	0.10545	-749.385179	0.066009	-749.448127	-750.365744
Benzothiophene	-705.748773	0.115291	-705.623386	0.044624	-705.668008	-706.5512789
Alkyl_product-enol	-897.296837	0.181404	-897.098491	0.061851	-897.158358	-898.4541917
Alkyl_product-keto	-897.309024	0.180877	-897.111451	0.062878	-897.171332	-898.4612764
product-olefin	-896.097731	0.158321	-895.923504	0.059588	-895.981304	-897.2420066
Int1	-1745.281907	0.514253	-1744.7196	0.135085	-1744.84308	-1748.226272
a-Int1	-1994.689987	0.476741	-1994.16793	0.126964	-1994.28527	-1997.599911
a-TS1	-1994.669752	0.471698	-1994.153037	0.127585	-1994.270341	-1997.574293
a-TS1'	-1994.669681	0.471994	-1994.15275	0.126894	-1994.26979	-1997.573529
a-TS1''	-1994.669809	0.471868	-1994.153	0.126524	-1994.26989	-1997.572874
a-TS1'''	-1994.667197	0.471807	-1994.15036	0.127588	-1994.26765	-1997.571418
a-TS1a	-1994.6723	0.472141	-1994.15549	0.12496	-1994.27138	-1997.573298
b-TS1	-1994.669787	0.471772	-1994.15317	0.125236	-1994.26943	-1997.573820
b-TS1'	-1994.667898	0.471637	-1994.15122	0.127582	-1994.26851	-1997.572215
b-TS1''	-1994.667515	0.471849	-1994.15083	0.125348	-1994.26719	-1997.571914
b-TS1'''	-1994.667579	0.471655	-1994.15085	0.127817	-1994.26826	-1997.571609
a-Int2	-1994.698495	0.477838	-1994.17511	0.129804	-1994.29381	-1997.603887
a-Int3	-2187.441458	0.564793	-2186.822761	0.146049	-2186.956838	-2190.714843
a-Int3_Ag	-2744.247666	0.584531	-2743.599097	0.171586	-2743.754749	-2747.994595
a-TS2	-2187.41602	0.56311	-2186.799298	0.146731	-2186.933065	-2190.689388
a-TS2_Ag	-2744.235464	0.583336	-2743.58862	0.170935	-2743.743443	-2747.978266
a-Int4	-2187.474251	0.566682	-2186.854773	0.142956	-2186.986253	-2190.741518
a-Int4_Ag	-2744.290457	0.58552	-2743.641771	0.168489	-2743.795252	-2748.03464
a-TS3_cis	-2187.442514	0.561953	-2186.82792	0.143182	-2186.959533	-2190.71186
a-TS3_trans	-2187.440346	0.56188	-2186.825878	0.142513	-2186.957017	-2190.710276
a-TS3'_cis	-2187.437518	0.562271	-2186.822361	0.145151	-2186.955056	-2190.707535
a-TS3'_trans	-2187.432844	0.561293	-2186.81812	0.148663	-2186.95281	-2190.707999
a-Int5_cis	-2187.444846	0.563271	-2186.828113	0.147195	-2186.96227	-2190.715866
a-Int5_trans	-2187.442325	0.563059	-2186.82578	0.146749	-2186.95964	-2190.714635

a-Int5' <i>cis</i>	-2187.441451	0.563987	-2186.824166	0.144328	-2186.957042	-2190.710612
a-Int5' <i>trans</i>	-2187.443592	0.563613	-2186.82654	0.145675	-2186.96012	-2190.71493
Int6	-3282.974404	0.437009	-3282.4891	0.13752	-3282.6143	-3285.81503
Int7	-3282.98458	0.436028	-3282.499	0.14196	-3282.6278	-3285.819545
Int8	-1846.952501	0.399858	-1846.506754	0.133507	-1846.628303	-1849.53612
Int9	-1846.943488	0.401743	-1846.495426	0.136656	-1846.618862	-1849.535016
Int10	-1995.881775	0.496427	-1995.33837	0.129152	-1995.458295	-1998.797633
Int11	-1746.488647	0.533772	-1745.905413	0.135289	-1746.030578	-1749.434372
a-TS4	-2187.401655	0.557759	-2186.790422	0.144178	-2186.92337	-2190.669139
a-Int6	-2187.422453	0.559526	-2186.809249	0.143375	-2186.942121	-2190.692182
a-Int7	-2186.271265	0.543583	-2185.675388	0.142162	-2185.806343	-2189.531448
a-TS5	-2186.220455	0.536558	-2185.631858	0.143096	-2185.762863	-2189.476676
a-Int8	-2186.250227	0.540075	-2185.657763	0.14247	-2185.789006	-2189.506946

18. References for Computational Section:

Full reference Gaussian 16:

Gaussian 16, Revision B.01, Frisch, M. J.; Trucks, G. W.; Schlegel, H. B.; Scuseria, G. E.; Robb, M. A.; Cheeseman, J. R.; Scalmani, G.; Barone, V.; Mennucci, B.; Petersson, G. A.; Nakatsuji, H.; Caricato, M.; Li, X.; Hratchian, H. P.; Izmaylov, A. F.; Bloino, J.; Zheng, G.; Sonnenberg, J. L.; Hada, M.; Ehara, M.; Toyota, K.; Fukuda, R.; Hasegawa, J.; Ishida, M.; Nakajima, T.; Honda, Y.; Kitao, O.; Nakai, H.; Vreven, T.; Montgomery Jr., J. A.; Peralta, J. E.; Ogliaro, F.; Bearpark, M.; Heyd, J. J.; Brothers, E.; Kudin, K. N.; Staroverov, V. N.; Kobayashi, R.; Normand, J.; Raghavachari, K.; Rendell, A.; Burant, J. C.; Iyengar, S. S.; Tomasi, J.; Cossi, M.; Rega, N.; Millam, J. M.; Klene, M.; Knox, J. E.; Cross, J. B.; Bakken, V.; Adamo, C.; Jaramillo, J.; Gomperts, R.; Stratmann, R. E.; Yazyev, O.; Austin, A. J.; Cammi, R.; Pomelli, C.; Ochterski, J. W.; Martin, R. L.; Morokuma, K.; Zakrzewski, V. G.; Voth, G. A.; Salvador, P.; Dannenberg, J. J.; Dapprich, S.; Daniels, A. D.; Farkas, Ö.; Foresman, J. B.; Ortiz, J. V.; Cioslowski, J.; Fox, D. J. Gaussian, Inc., Wallingford CT, 2016.

1. Frisch, M. J. .; Trucks, G. W. .; Schlegel, H. B. .; Scuseria, G. E. .; Robb, M. A. .; Cheeseman, J. R. .; Scalmani, G. .; Barone, V. .; Petersson, G. A. .; Nakatsuji, H. .; et al. Gaussian 16, Revision B.01. 2016.
2. Yu, H. S.; He, X.; Li, S. L.; Truhlar, D. G. MN15: A Kohn–Sham Global-Hybrid Exchange–Correlation Density Functional with Broad Accuracy for Multi-Reference and Single-Reference Systems and Noncovalent Interactions. *Chem. Sci.* **2016**, 7 (8), 5032–5051.

3. Weigend, F.; Ahlrichs, R. Balanced Basis Sets of Split Valence, Triple Zeta Valence and Quadruple Zeta Valence Quality for H to Rn: Design and Assessment of Accuracy. *Phys. Chem. Chem. Phys.* **2005**, *7* (18), 3297–3305.
4. Weigend, F. Accurate Coulomb-Fitting Basis Sets for H to Rn. *Phys. Chem. Chem. Phys.* **2006**, *8* (9), 1057–1065.
5. Rappoport, D.; Furche, F. Property-Optimized Gaussian Basis Sets for Molecular Response Calculations. *J. Chem. Phys.* **2010**, *133* (13), 134105.
6. Andrae, D.; Häußermann, U.; Dolg, M.; Stoll, H.; Preuß, H. Energy-Adjusted ab Initio Pseudopotentials for the Second and Third Row Transition Elements. *Theor. Chim. Acta* **1990**, *77* (2), 123–141.
7. Marenich, A. V.; Cramer, C. J.; Truhlar, D. G. Universal Solvation Model Based on Solute Electron Density and on a Continuum Model of the Solvent Defined by the Bulk Dielectric Constant and Atomic Surface Tensions. *J. Phys. Chem. B* **2009**, *113* (18), 6378–6396.
8. Ebersson, L.; Hartshorn, M. P.; Persson, O.; Radner, F. Making Radical Cations Live Longer. *Chem. Commun.* **1996**, No. 18, 2105–2112.
9. Gu, X.; Song, X.; Shao, C.; Zeng, P.; Lu, X.; Shen, X.; Yang, Q. Electrospinning of Poly(Butylene-Carbonate): Effect of Solvents on the Properties of the Nanofibers Film. *Int. J. Electrochem. Sci.* **2014**, *9* (12), 8045–8056.
10. Carraro, M.; Gardan, M.; Sartorel, A.; Maccato, C.; Bonchio, M. Hydrogen Peroxide Activation by Fluorophilic Polyoxotungstates for Fast and Selective Oxygen Transfer Catalysis. *Dalt. Trans.* **2016**, *45* (37), 14544–14548.
11. Sigma-Aldrich. 1,1,1,3,3,3-Hexafluoro-2-propanol
<https://www.sigmaaldrich.com/catalog/product/aldrich/105228> (accessed Jun 6, 2017).
12. Abraham, M. H.; Andonian-Haftvan, J.; Whiting, G. S.; Leo, A.; Taft, R. S. Hydrogen Bonding. Part 34. The Factors That Influence the Solubility of Gases and Vapours in Water at 298 K, and a New Method for Its Determination. *J. Chem. Soc. Perkin Trans. 2* **1994**, No. 8, 1777–1791.
13. Richmond, E.; Yi, J.; Vuković, V. D.; Sajadi, F.; Rowley, C. N.; Moran, J. Ring-Opening Hydroarylation of Monosubstituted Cyclopropanes Enabled by Hexafluoroisopropanol. *Chem. Sci.* **2018**, *9* (30), 6411–6416.
14. Berkessel, A.; Adrio, J. A. Dramatic Acceleration of Olefin Epoxidation in Fluorinated Alcohols: Activation of Hydrogen Peroxide by Multiple H-Bond Networks. *J. Am. Chem. Soc.* **2006**, *128* (41), 13412–13420.

15. Winget, P.; Dolney, D. M.; Giesen, D. J.; Cramer, C. J.; Truhlar, D. G. Minnesota solvent descriptor database <https://comp.chem.umn.edu/solvation/mnsddb.pdf> (accessed Mar 15, 2022).
16. Grimme, S. Supramolecular Binding Thermodynamics by Dispersion-Corrected Density Functional Theory. *Chem.: Eur. J.* **2012**, *18* (32), 9955–9964.
17. Funes-Ardoiz, I.; Paton, R. S. GoodVibes v1.0.1 <http://doi.org/10.5281/zenodo.56091>.
18. Schrödinger, L. *The PyMOL Molecular Graphics Development Component, Version 1.8*; 2015.